Shear driven crack arrest investigation under compressive state: Prediction of fretting fatigue failure of aluminium strands

Julien Said, Siegfried Fouvry, Georges Cailletaud, Christine Yang, Fikri Hafid

Shear driven crack arrest investigation under compressive state: prediction of fretting fatigue failure of aluminium strands

Julien Said[a,b,c,*], Siegfried Fouvry[a,*], Georges Cailletaud[c], Christine Yang[b], Fikri Hafid[b]

[a)] Ecole Centrale de Lyon, UDL Univ. De Lyon, LTDS-CNRS 5513, 36 Avenue Guy de Collongue, 69134, Ecully, France

[b)] RTE – Direction de la R&D – Pôle Smartlab, 92073, Paris la Defense Cedex, France

[c)] MINES ParisTech, PSL Research University, MAT-Centre des Matériaux, CNRS UMR 7633, BP87, 91003, Evry, France

*: Corresponding authors at: Ecole Centrale de Lyon, UDL Univ. De Lyon, LTDS-CNRS 5513, 36 Avenue Guy de Collongue, 69134, Ecully, France (J. Said). E-mail addresses: julien.said@ec-lyon.fr (J. Said), Siegfried.fouvry@ec-lyon.fr (S. Fouvry).

Key words: Fretting fatigue; crack arrest; Stress Intensity Factors; aluminium; mode II mechanisms

Abstract: Fretting fatigue crack propagation in aluminium strands was investigated through experimental tests and FEM simulations. Fretting fatigue tests revealed that crack nucleation predictions are not sufficient to fully predict the total strand failure, and crack arrest conditions may be reached for nucleated cracks. The geometry of arrested cracks was characterized and used to perform simulations using FEM in order to dedude Stress Intensity Factor (SIF) distributions along the crack front. These results showed that even in a fully compressive state, cracks are still able to propagate to a certain extent, and a mode II SIF threshold has been proposed.

1. Introduction

The lifetime assessment of overhead conductors is becoming a key point for any Transmission System Operator (TSO) in charge of a power grid. In order to adapt their maintenance and repair protocols, they need to be able to predict the mechanical behavior of their power lines with physical comprehension.

Among all the damaging loadings that affect the total lifetime of a conductor, the one addressed in this work is fretting fatigue. A typical conductor is a wire rope assembly, constituted of several layers of helical strands (figure 1a) that can be made of steel, aluminium alloys or quasi-pure aluminium. When this complex assembly is subjected to external loadings such as wind vibrations, it may cause a small oscillatory movement within all the contacts between neighboring strands. This specific tribological load is defined as fretting, and the combination of this phenomenon with the fatigue induced by the conductor's motion results in fretting fatigue. In such a configuration, fretting nucleates cracks in the contact zone, and the fatigue bulk stress propagates these cracks until total failure.

It has been frequently reported in the literature that this process reduces the total lifetime of overhead conductors [1]–[4] . Moreover, studies are widely focused on the clamping zone, as most of the strand failures observed on the grid were located in this particular area (figure 1c) [5], [6]. Thus, in a previous work, a numerical and experimental strategy has been proposed to predict the crack nucleation risk within a conductor subjected to both the clamping force and an oscillating bending movement [7]. This work was also specifically focused on the contacts between the two aluminium outer layers. To achieve this prediction, two numerical models have been developed: a macroscopic model, as it has also been proposed in other studies [8]–[10], as well as a local model [11], [12]. The introduced macroscopic model represents a full portion of a conductor and its interactions with a clamp (figure 1b), using volume hexahedra elements and the ABAQUS Explicit solver. Even if this model has a high computational cost and isn't suitable with implicit calculations, it is easy to handle and is meant to give a first evaluation of the fretting

loading conditions between the aluminium strands. On the other hand, the local model stands for a single contact between two individual strands. It also uses volume hexahedra elements with a refined mesh in the contact zone, and is suitable with implicit calculation.

The crack nucleation prediction was achieved using the Crossland multiaxial fatigue criterion associated with a non-local critical distance l_{opt} approach, as previously applied by several authors [13]–[16]. These numerical predictions were then compared to experimental results obtained using a dedicated fretting fatigue test bench that recreates the exact same conditions. These comparisons revealed that the numerical strategy manages well to predict the occurrence of crack at the contact edges, and the higher the equivalent Crossland stress is, the longer the cracks would be. However, it has also been observed that the presence of such cracks is not enough to conclude whether the strand will display total failure or not. Finally, further numerical analyses showed a possible strong link between an increase of normal force and the propagation behavior, with high compressive stress around the crack tip. This stands as the starting point of the current analysis. Only considering crack nucleation may not be enough to predict comprehensively the total failure of an aluminium strand under fretting fatigue loading. Thus, the proposed work investigates crack propagation with crack closure effects, induced by compressive hydrostatic pressure. Fretting fatigue tests were carried out to study experimental crack arrests conditions, and numerical simulations were achieved with a fully meshed crack to proceed to Stress Intensity Factors (SIF) calculations. The main purpose of this study is to propose a SIF based criterion in order to predict the crack arrest phenomenon.

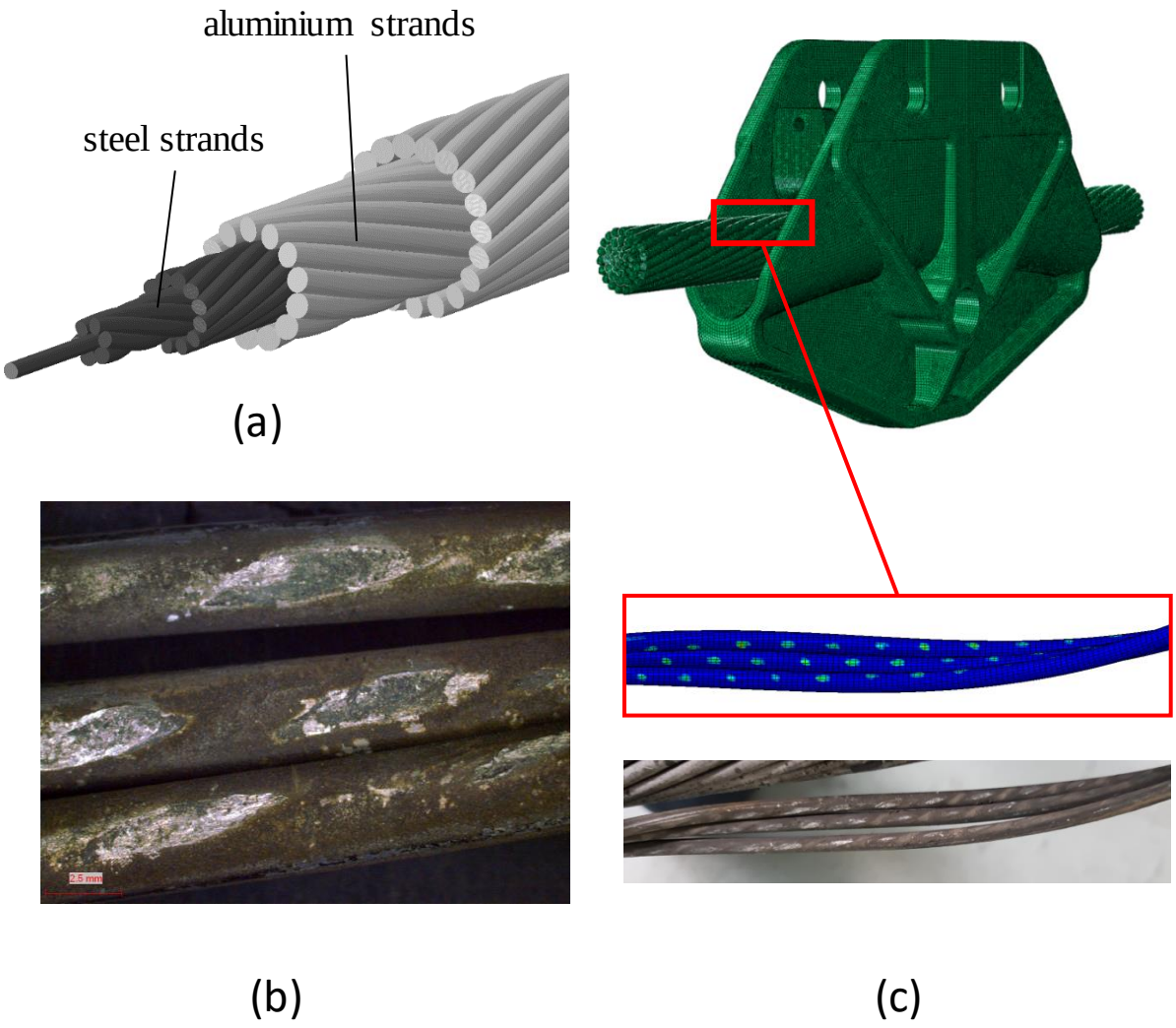

Figure 1 (a) 3D rendered view of an Aluminium Conductor Steel Reinforced (ACSR) structure, with inner steel layers and outer aluminium layers; (b) close-up view of potential fretting scar observed in a clamping zone; (c) fully meshed conductor-clamp assembly used for the global FEM model;

2. Crack nucleation prediction on a single contact

As mentioned in the introduction, a previous research work has been conducted to propose a prediction of the crack nucleation risk within an aluminium-aluminium mono contact. Thus, this section will sum up the main results from these previous predictions and highlight the conclusions that led to investigate further the crack arrest phenomenon.

2.1. Conductor and material

Most elder power lines use Aluminium Steel Reinforced Conductors (ACSR, figure 1a) with aluminium strands (purity >99%) for electricity transportation and steel strands to ensure the mechanical strength of the conductor. These aging lines are the most likely to be replaced by the next decade, which is why the study focuses on this specific type of conductor. Even among ACSR, various designs and geometry exist. The current study focuses on one specific conductor geometry, with the following characteristics: 3.6 mm of diameter for all aluminium strands while the steel strands diameter is 2.40 mm. Because of their respective lay angles, the resulting configuration corresponds to a crossed cylinder system with a total relative angle of $\beta = 30°$. This choice was motivated by the observation that nearly no failure was observed on steel strands on the French grid during service. All samples used for experimental testing were taken from a dedicated spool of aluminium strands without their helical shape to avoid successive manual handling. This handling would induce additional plastic strain and residual stresses within the strands and may ultimately affect the results.

2.2. Numerical local modeling using Finite Element Analysis (FEA)

2.2.1. FEA model description

The numerical strategy relies on a 3D model represented in figure 2a. The crossed-cylinder configuration is obtained using two half-cylinders to represent the aluminium strands, and are meshed the same way. This first model used hexahedra volume elements and ran with the ABAQUS/Implicit solver. Both the augmented Lagrangian and Penalty algorithms were tested to describe the contact behavior, and gave systematically extremely similar results. Thus, most of the results presented throughout this study were obtained using the Penalty algorithm. It can also be mentioned that this local modelling considers straight strands, while the actual material has a helical shape, depending on its layer. However, this work focuses on the aluminium layer, which displays the lower local curvature and longer laying period (> 160 mm).

Considering that a modeled strand is 6 mm long in this model, the influence of the helical shape was considered negligible for this work.

While the upper strand applies the fretting loading (i.e. the tangential and normal loads), the fatigue bulk stress is applied on one end of the lower strand. These boundary conditions are applied through reference points during three distinct time steps (figure 2b) throughout a single simulation:

-Step (1): a very small vertical displacement is applied on the upper strand to initiate the contact and ensure the stability of the next steps (especially when the Augmented Lagrangian algorithm is used)

-Step (2): the static normal force P is imposed on the upper strand while the mean value for the fatigue bulk stress is applied on the lower part.

-Step (3): the normal force remains constant while the tangential and fatigue loadings $Q(t)$ and $\sigma(t)$ describe a sinusoidal cycle.

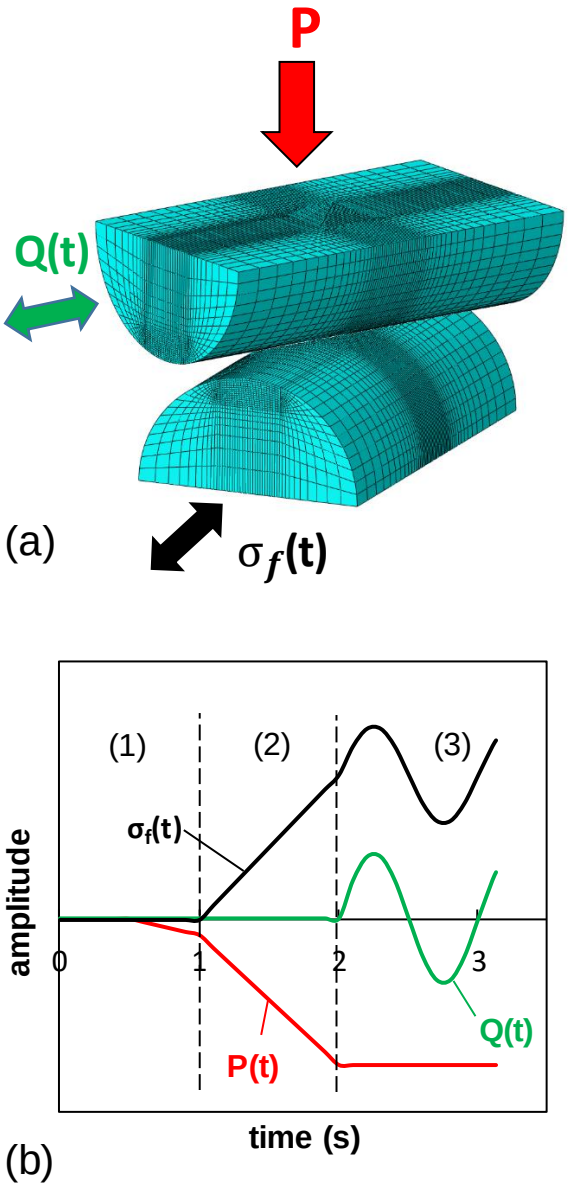

Figure 2: Local model mesh grid modelling a single contact between two aluminium strands; (b): timeframe used for all fretting fatigue simulations

This model considers an isotropic and elastic material, for which the Young's modulus E = 65 GPa and Poisson ratio ν = 0.34 were experimentally identified. The partial-to-gross slip transition coefficient μ_t = 1.1 was measured using the same procedure as described in [7], this time specifically in fretting fatigue. Because of the aluminium softness, it would be relevant to take into account plasticity in the model.

However, adding more non-linearity to this 3D problem with contact makes the convergence with the implicit solver more difficult. Another key aspect of a fretting contact concerns the gradient effects. Fretting is characterized by severe stress gradients that imply to consider a non-local fatigue stress analysis. The critical distance approach is currently applied, using a reverse post-processing analysis of plain fretting experiments to find the critical distance l_{opt} = 130 µm [7]. By considering a subsurface stress state (reaching quasi elastic stress conditions) the given critical distance fatigue stress analysis is in fact less affected by plasticity and gradient effects and the proposed 3D elastic investigation remains representative.

Figure 3 shows a typical crack nucleation risk distribution [17], [18], which shows the location of the hotspots where cracks are more likely to initiate. This crack nucleation risk is evaluated by comparing the equivalent Crossland stress σ_C with the torsion fatigue limit noted τ_d. Moreover, σ_C also depends on the tension/compression fatigue limit noted σ_d, and is expressed as follows:

$$\sigma_c = \sqrt{J_{2,a}} + \alpha_C . \sigma_{H,max} \quad (1)$$

With $\alpha_C = \frac{\tau_d - \sigma_d/\sqrt{3}}{\sigma_d/\sqrt{3}}$

$J_{2,a}$ represents the second invariant of the deviatoric stress amplitude during a loading cycle, and $\sigma_{H,max}$ is the maximum hydrostatic stress σ_H during the same cycle. The two fatigue limits were identified using plain fatigue tests as described in [7]. According to the Crossland criterion, there is crack nucleation thus risk of failure when $\sigma_C \geq \tau_d$.

Besides the crack nucleation prediction, figure 3b focuses on the multiaxiality aspect usually inherent in a fretting contact. The triaxiality ratio η, defined as the ratio between the hydrostatic stress σ_H and the Von Mises equivalent stress σ_{VM}, was computed in the contact zone at Q = +Q* and Q = -Q*. As a reference, it can be noted that η = 0.33, η = 0 and η = -0.33 correspond to plain tension, plain shear and plain

compression, respectively. From these distributions, it can be observed that the triaxiality is stronger in the volume beneath the contact edges, where the cracks are systematically located.

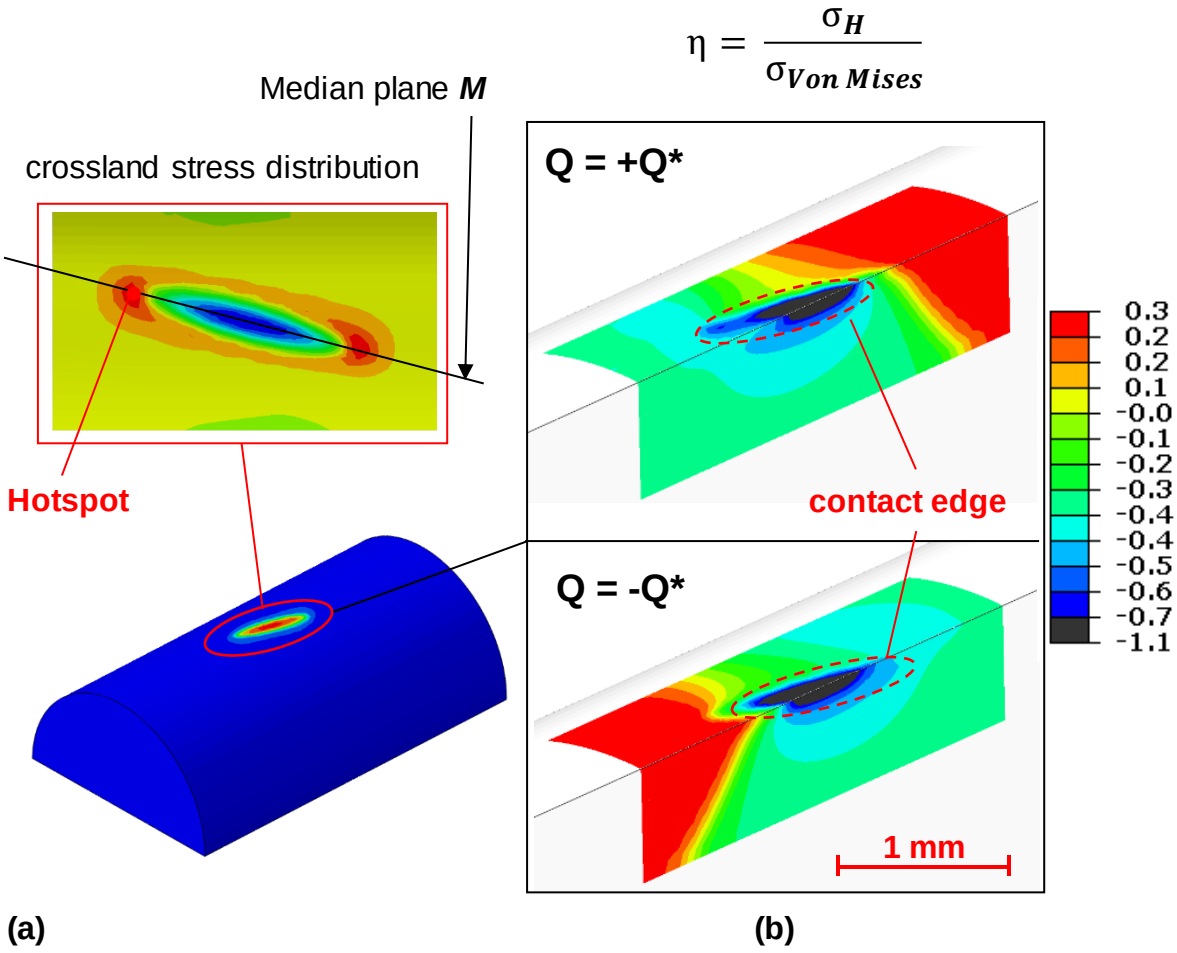

Figure 3(a): Typical Von Mises stress distribution in the contact with a close-up view of the Crossland stress distribution (Q = 150 N, P = 200 N) on the contact surface. Hotspots are located at the edges of the contact; (b): overview of a cross-section of the triaxiality ratio η distribution at Q = +Q and Q = -Q**

2.2.2. Application to crack nucleation risk assessment and link to failure

With this local model calibrated to predict the crack nucleation risk at the hotspots, the following step consists in applying it to fretting fatigue loadings extracted from the global model illustrated figure 1b. As the description of this macroscopic model is not a topic of the current study, only the corresponding outputs will be considered here. Five representative loading cases were selected to account for as many

fretting fatigue configurations as possible, and the associated conditions are listed in table 1. All these cases are considered as realistic conditions, which is why they are relevant to investigate.

Table 1: Description of five realistic fretting fatigue loading conditions

LOADING CASE	**P (N)**	**Q* (N)**	$\sigma_{f,max}$ **(MPA)**
1	71	17	99
2	117	41	35
3	320	70	60
4	777	199	3
5	64	18	98

Based on these conditions, the local model described in the previous section has been used to simulate the same configurations. Then, the equivalent Crossland stress σ_C was computed below the hotspot at the critical distance l_{opt} and compared to the torsion fatigue limit τ_d. The corresponding results are displayed figure 4, and highlight the fact that 4 configurations among 6 are likely to nucleate thus to ultimately fail according to the current numerical methodology.

The final step of the initial strategy was to test these conditions experimentally using a dedicated fretting fatigue test bench that will be presented in detail in the next section. This bench is meant to recreate the single contact configuration between two aluminium strands and is illustrated in figure 5. The associated tests that were conducted to recreate the same loading cases revealed two key points:

- No total failure was observed on all 5 cases after 10^7 cycles of fretting fatigue

- Optical analyses on processed samples revealed the occurrence of cracks for cases 2, 3 and 4, as predicted by the Crossland criterion, while nothing was observed on cases 1 and 5.

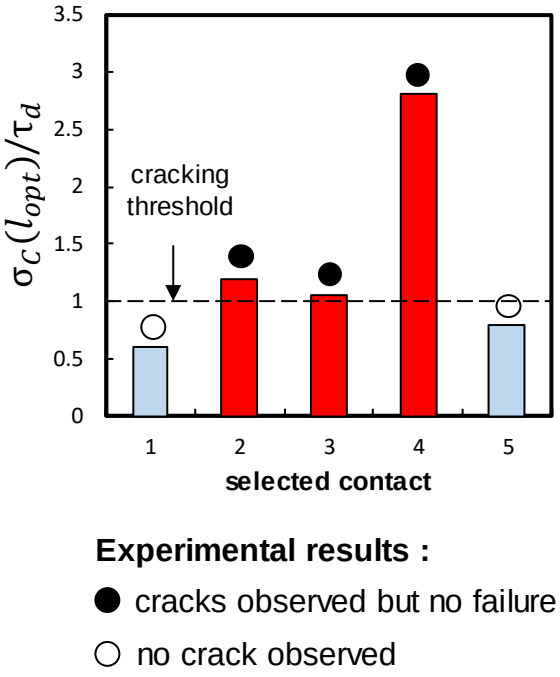

Figure 4 comparisons between FEM critical distance Crossland stress analyis (l_{opt} = 130 µm) and experiments

This presence of cracks associated with the absence of total failure even after 10^7 cycles strongly suggests that there may be a crack arrest phenomenon involved. This new hypothesis implies that the sole consideration of the crack nucleation risk is not sufficient to fully predict the fretting fatigue response of the considered material, and the crack propagation behavior needs to be addressed. The following details will focus on the investigations achieved on this topic, with a special attention given to the influence of the fretting normal load. The goal of the present work is to complete the initial crack nucleation strategy by identifying a Stress Intensity Factor (SIF) threshold to account for possible crack arrest phenomena.

3. Experimental crack arrest investigation and normal force effects

3.1. Experimental setup

The hydraulic fretting fatigue rig used for this work was initially designed to recreate the same conditions as those predicted by the numerical strategy described in the previous section. However, thanks to its double actuator configuration, it is perfectly suited to investigate various behaviors by controlling fretting and fatigue separately. The lower actuator (figure 5a) is force controlled and imposes the fatigue loading $\sigma_f(t)$, while the upper actuator is displacement controlled to ensure the test stability. The tangential force is measured using two force sensors: one placed at each end of the fatigue sample. Then, the tangential force $Q_{diff}(t)$ corresponds to the difference between the two forces. If there is no contact, both sensors will measure the same value (the fatigue loading) and their difference will be null. For each test, the frequency was fixed at 20 Hz for a limit lifetime of 10^7 cycles.

Figure 5c represents how the vertical fatigue sample is loaded. The fretting contact is obtained using a separate and shorter aluminium strand with the relative angle $\beta = 30°$. To avoid any bending, a counter body is placed on the opposite side of the fatigue sample. This counter body consists in a PTFE polymer, which displays a very low partial-to-gross slip transition coefficient against aluminium. Prior to the fretting fatigue tests that will be discussed in the following section, tests with two PTFE-aluminium contacts were conducted to characterize the fretting response for this kind of contact. From these preliminary tests, it was deduced that one PTFE-aluminium contact has a friction coefficient $\mu_{PTFE/al}$ =0.04. It means that for P = 200 N, the PTFE-aluminium contact induces less than 10 N whatever the slipping regime. This value was kept in mind for all following fretting fatigue tests, and the actual Q* corresponding to the aluminium/aluminium contact would be deduced as follows:

$$Q^* = Q^*_{diff} - \mu_{PTFE/al}.P \quad (2)$$

While the lower actuator applies the fatigue loading, the fretting displacement amplitude δ(t) is manually increased until the tangential force Q* reaches the targeted value.

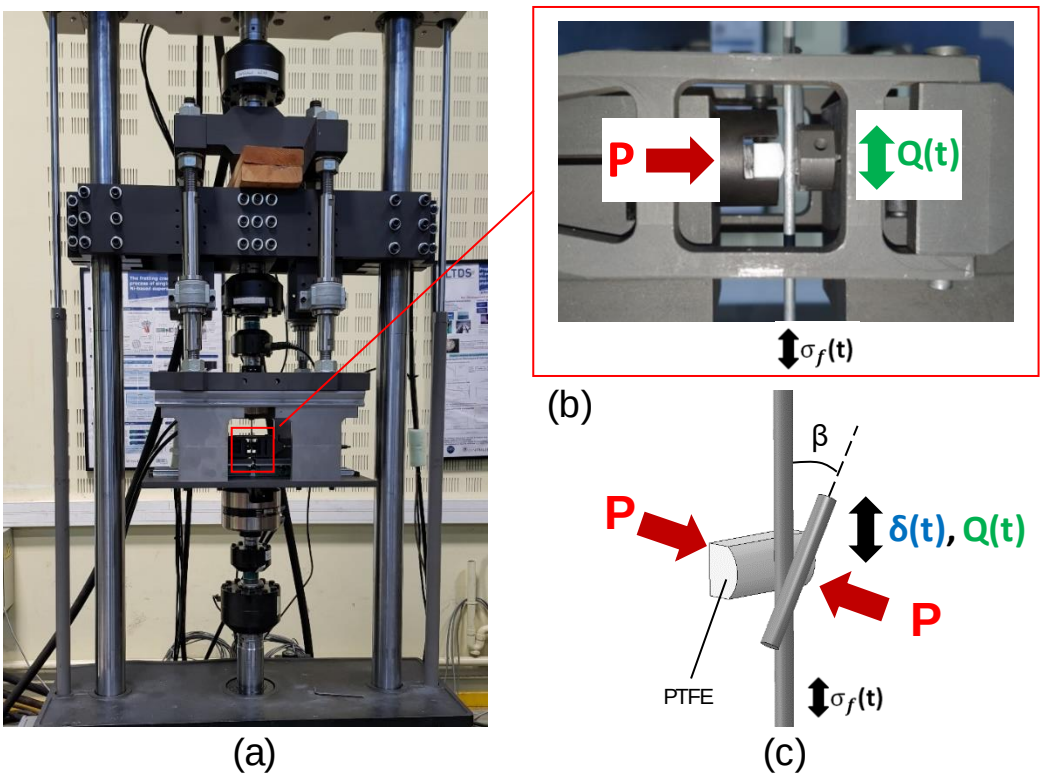

Figure 5 (a): double actuator fretting fatigue rig used; (b): close up view of the contact area; (c) schematic view of the contact zone

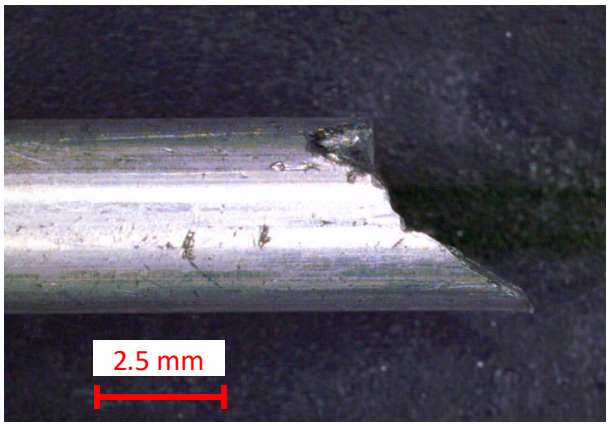

Figure 6: failed aluminium strand tested in fretting fatigue (Q= 150 N, P=200 N, σ_{fmax} = 60 MPa, R = 0.5)

3.2. Results and influence of normal force

Four series of tests were performed, and all the corresponding conditions are listed in table 2. For all tests, the fatigue loading ratio $R = \sigma_{f,min}/\sigma_{f,max}$ was fixed at R = 0.5. Figure 7 plots the results obtained and shows how the fretting fatigue life of a strand is affected by an increase of normal force P. The two fatigue loadings tested were chosen to get the most significant results. Lower fatigue stresses, for example $\sigma_{f,max}$ < 50 MPa, would not ensure strand failure within 10^7 cycles even with high tangential forces. On the contrary, it has been witnessed that $\sigma_{f,max}$ > 80 MPa may induce plain fatigue failures around the upper fatigue jaw. For the fatigue stresses listed in table 1, failures were systematically located in the contact area.

Table 2: list of all fretting fatigue conditions tested, with associated lifetimes

$\sigma_{f,max}$ (MPa) R = 0.5	Q (N)	P (N)	Lifetime (10^6 cycles)
60	150	150	**3**
60	150	200	**3.2**
60	150	250	**6**
60	150	275	**9.5**
60	150	300	**>10**
60	150	320	**>10**
60	200	300	**3.3**
60	200	350	**2.8**
60	200	400	**2.4**
60	200	410	**3.1**
60	200	420	**7.8**
60	200	450	**>10**
60	200	470	**>10**
70	150	150	**4.4**
70	150	200	**2.3**
70	150	210	**2.4**
70	150	230	**9.2**
70	150	250	**>10**
70	150	300	**>10**
70	200	350	**3.9**
70	200	400	**3**
70	200	415	**3.5**
70	200	450	**>10**
70	200	470	**>10**

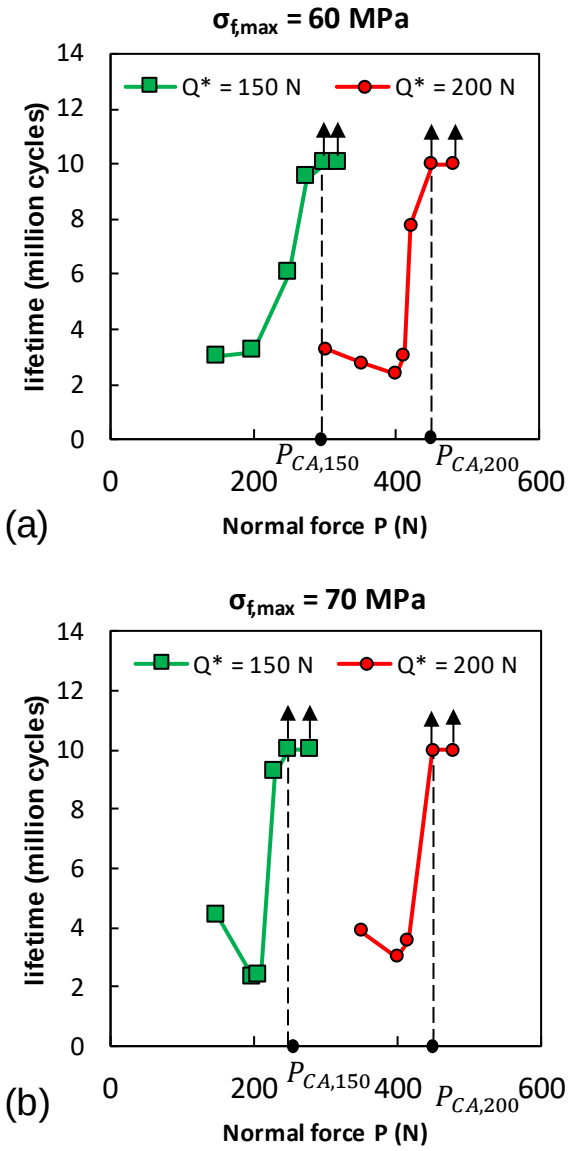

Figure 7 (a): fretting fatigue lifetime evolution versus the normal force P for $\sigma_{f,max}$ = 60 MPa; fretting fatigue lifetime evolution versus the normal force P for $\sigma_{f,max}$ = 70 MPa

These plots illustrate the concrete influence of the normal force and hydrostatic pressure on the actual fretting fatigue life of aluminium strands. It shows how an increase of the normal force, while keeping all other parameters constant, can delay or prevent the strand failure. It may also be noticed that there seem to be a threshold effect: while P remains below a threshold normal force noted P_{CA}, the lifetime evolution doesn't seem deeply affected. Then, when P gets near this threshold P_{CA}, the lifetime before failure exhibits a sharp increase, as it can be seen especially for tests with $\sigma_{f,max}$ = 60 MPa (figure 7a).

Eventually, for $P \geq P_{CA}$ the strand lifetime is higher than 10^7 cycles. This specific behavior suggests once again that an increase of normal force and compressive hydrostatic pressure may be related to crack arrest and closure effects. Another interesting observation coming from these data concerns the experimental lifetimes for $P < P_{CA}$. Whatever the fatigue and tangential loadings, the fretting fatigue life to failure is stable with most occurrences between 2 and 4 millions of cycles.

Table 3: normal force thresholds P_{CA} values for various fretting fatigue loadings

	$\sigma_{f,max}$ = 60 MPa	$\sigma_{f,max}$ = 70 Mpa
Q* = 150 N	P_{CA} = 300 N	P_{CA} = 250 N
Q* = 200 N	P_{CA} = 450 N	P_{CA} = 450 N

The most significant results extracted from these plots are the threshold values P_{CA} for the normal force, and are displayed in table 3. According to all four series of tests, the tangential force amplitude Q* has a way greater influence on this threshold than the fatigue stress σ_f. For Q* = 200 N, it remains the same at $P_{CA,200}$ = 450 N for both fatigue loads. For Q* = 150 N, fatigue has a slight influence with $P_{CA,150}$ ranging from 250 N for $\sigma_{f,max}$ = 60 MPa to $P_{CA,150}$ = 300 N for $\sigma_{f,max}$ = 70 MPa. Still, fatigue doesn't stand out as a key parameter for this threshold value. On the contrary, a raise of about 30% of tangential force Q induces an increase of 60 % for the crack arrest threshold P_{CA}. It suggests that the shear stress generated in the fretting contact has much more influence than the fatigue bulk stress. Further post-processing analyses of non-failed samples also revealed that the associated crack depths were systematically between 170 and 250 µm (figure 8). This tends to confirm that the crack arrest phenomenon is quickly reached in the contact zone, where fretting induced stresses are predominant compared to the fatigue stress. In addition to

these lengths, figure 8 also highlights the diving angle α that displays a rather low discrepancy among all observed nucleated cracks, with values close to $\alpha = 30°$. This consistency among all post-processed cracks helps to establish a typical crack geometry corresponding to the crack arrest state. This will be used in the next section with proper crack modeling. It is also interesting to note that the projected crack depths (b_{CA} = 200 – 250 µm) related to the crack arrest condition is nearly twice the critical distance l_{opt} = 130 µm. This experimental correlation seems to confirm the Taylor assumption and former $l_{opt} – b_{opt}$ stratey developed by Gandiolle et al [15]: $l_{opt} = b_{CA}/2$

With these data and especially the P_{CA} values, the next step is to proceed to Stress Intensity Factor calculations using finite element analysis and 3D modeling.

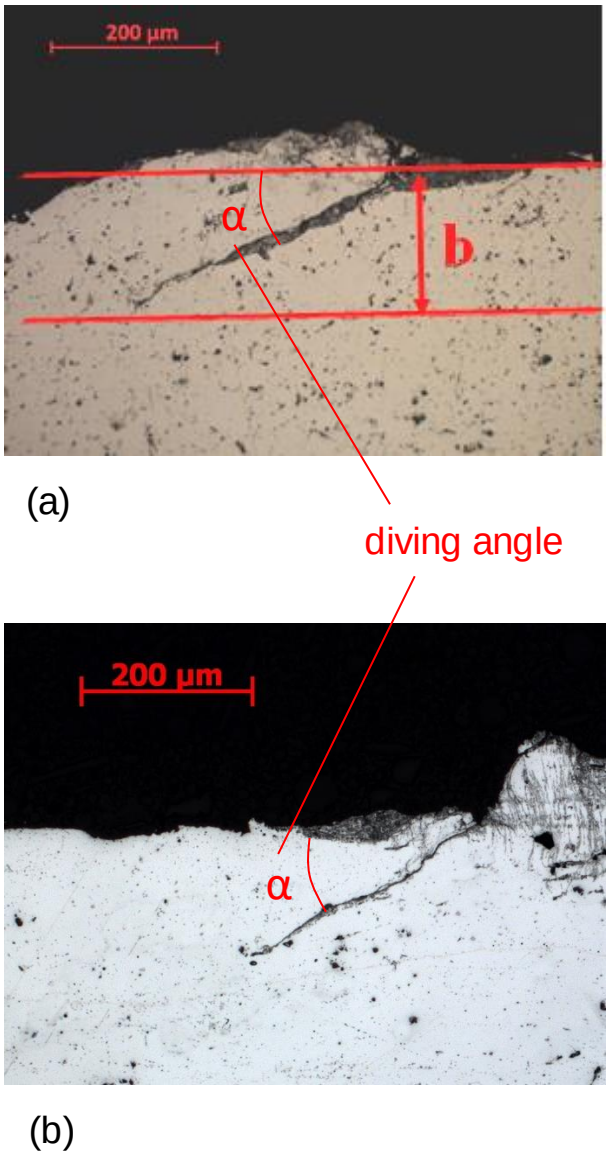

Figure 8 (a): cross-sectionnal observation along the contact median plane for Q = 200 N, P = 450 N, $\sigma_{f,max}$ = 70 MPa; (b) cross-sectionnal observation along the contact median plane for Q = 150 N, P = 300 N, $\sigma_{f,max}$ = 60 MPa

4. Numerical modeling of the propagation behavior

4.1. 3D model with embedded crack

In order to evaluate the Stress Intensity Factors along a crack tip in a fretting configuration, a crack geometry has to be considered in the previous 3D model. The chosen method to achieve that was to include a fully meshed crack inserted into the initial mesh, using the Z-cracks tool. Z-cracks is a part of the Z-set suite that allows to study the cracking behavior in various 3D configurations, and is suitable with FEA solvers like the ABAQUS/Implicit solver used in this work. In the following section, two tools from Z-cracks have been used:

- The remeshing utility. It can insert a user-defined crack geometry, insert a crack into a sane mesh and remesh the model only using tetrahedral elements. The newly created mesh is refined around the crack front to account for its inherent discontinuity. For this study, this tool takes as input both a crack geometry (figure 9a) and an ABAQUS templated input file. The output is then a new ABAQUS templated input file corresponding to the cracked model.
- The SIF post-processing utility: It computes the SIF distribution from Linear Elastic Fracture Mechanics (LEFM) along the crack tip. Fracture modes I, II and III are accounted by K_I, K_{II} and K_{III} respectively. This utility takes as input an FEA output database and returns SIF values along the crack front for every time frame available. The relations used for these calculations are expressed in the equations below.

The LEFM-based SIF processing is based on the energy release G. It is related to the SIFs following the IRWIN relation:

$$G = \frac{1-\nu^2}{E}\left(K_I^2 + K_{II}^2\right) + \frac{K_{III}^2}{2\mu}, \qquad \text{where } \mu = \frac{E}{2(1+\nu)} \tag{3}$$

G is then computed using the G – theta method [19], [20]. To deduce the values of K_I, K_{II} and K_{III} from this energy release rate, any pure mode I, II or III Westergaard displacement solution $v^{I,\ II,\ III}$ can be introduced. These solutions are associated with the corresponding virtual energy release rates $G^{v,\ I,\ II,\ III}$, which gives the following relations:

$$K_I = \sqrt{\frac{E}{1-\nu^2}\, G^{v,I}} \tag{4}$$

$$K_{II} = \sqrt{\frac{E}{1-\nu^2}\, G^{v,II}} \tag{5}$$

$$K_{III} = \sqrt{2\,\mu\, G^{v,III}} \tag{6}$$

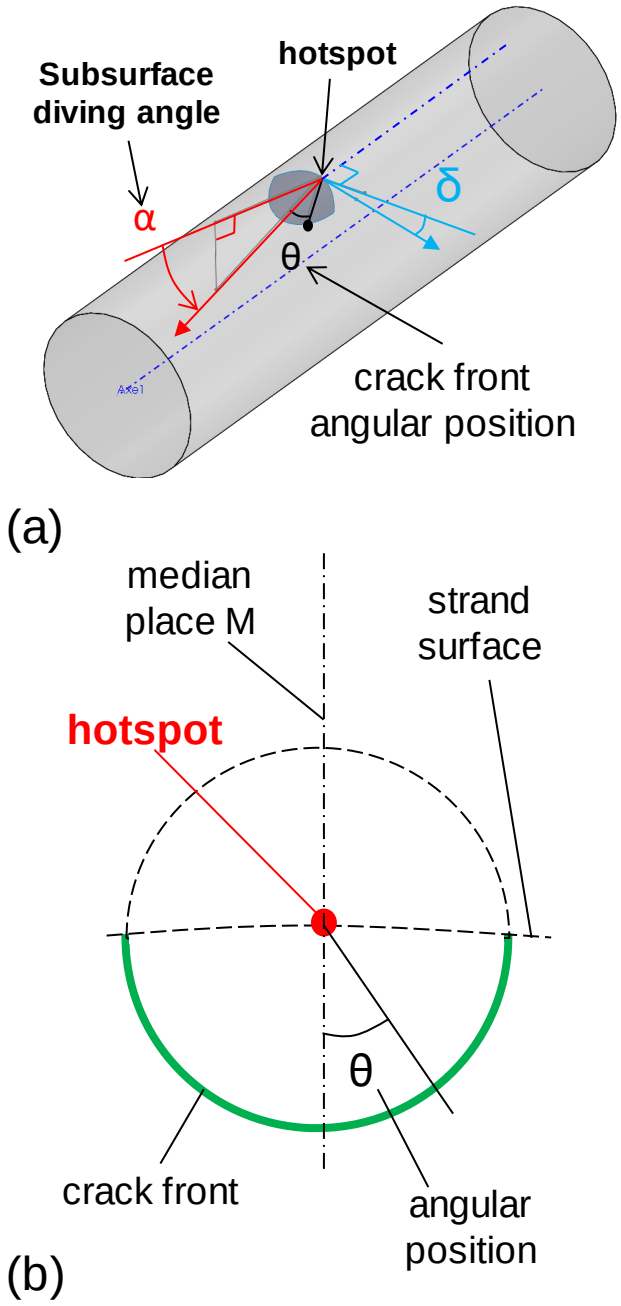

Figure 9(a): illustration of the geometric angles used to define the inserted crack; (b) close-up schematic view of the crack front and how the angular position θ is defined

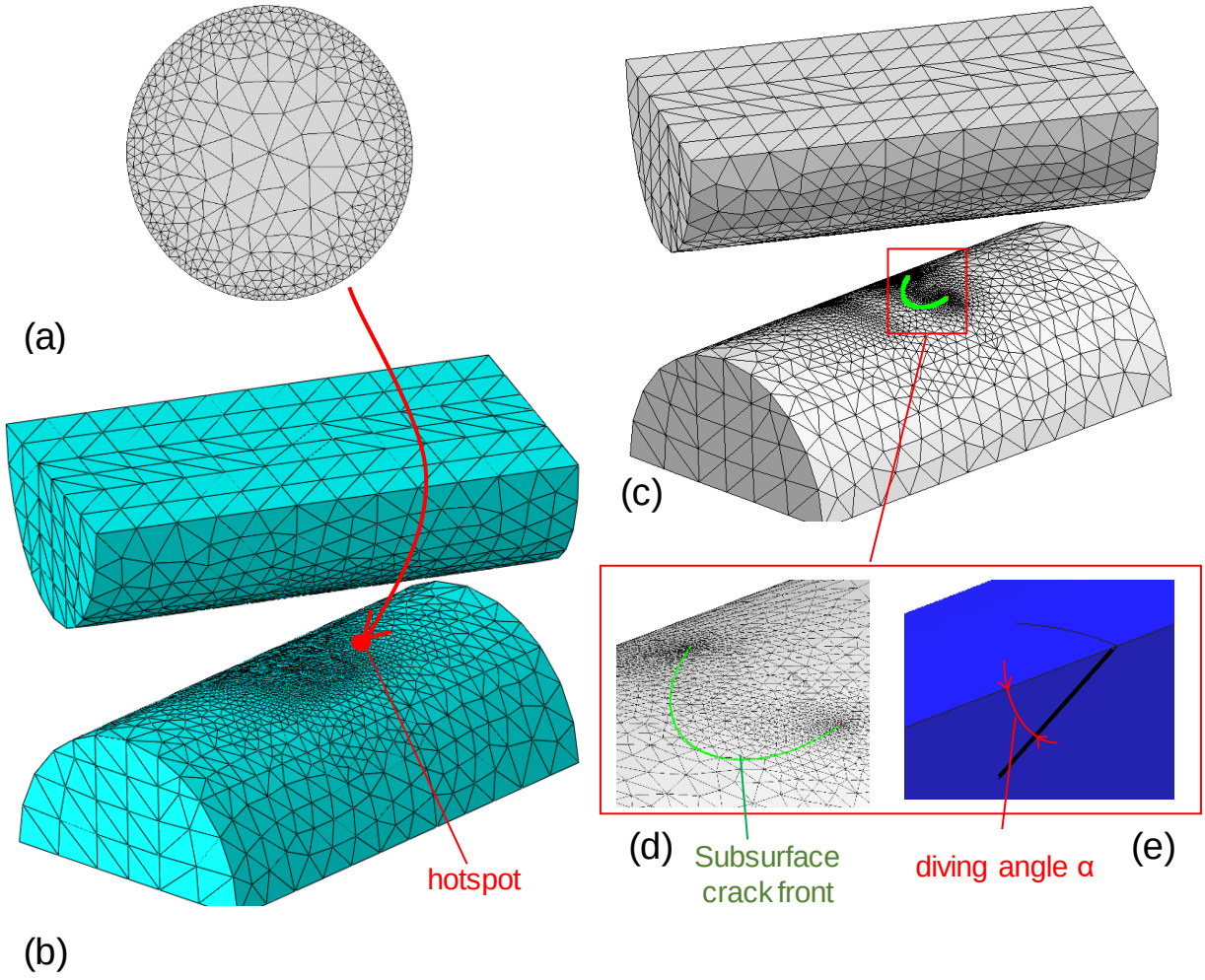

Figure 10: penny shaped crack mesh before insertion; (b) sane mesh before insertion; (c) cracked mesh and hotspot location; (d): close up view of the hotspot area with the highlighted crack front; (e) cross-sectionnal view at the crack location

The last key aspect of this modeling is the crack itself. The crack geometry described here is based on all experimental observations made on failed and unfailed strands after testing and described in section 3.2. Furthermore, these cracks do not seem to bifurcate even in fretting fatigue and on failed strands (figure 6), as it is often observed when propagation becomes only driven by the fatigue bulk stress. The explanation for this specific behavior may be related to microstructural and residual stress effects induced by the manufacturing process, and especially wire drawing. However, the purpose of the present work is not to propose a physical explanation for these orientations but rather investigate on the consequences of this

geometry in a fretting configuration. No outplane propagation criterion was used to try to predict the crack path: the fully-elastic and isotropic behavior used to describe the material would not be able to account for any effect of the microstructure or residual stress. Thus, the crack geometry used was directly based on experimental cracks observed on unfailed samples after 10^7 cycles (i.e. above the crack arrest threshold $P > P_{CA}$ illustrated in figure 7). Three distinct angles are used to describe the crack orientation, which are illustrated figure 9:

- The diving angle α already defined earlier based on optical observations. It was set to $\alpha = 30°$.
- To quantify the angle between the strand axis and the actual direction of propagation, δ was defined. Cracks propagate below the contact along the median plane M (figure 3) rather than along the strand axis. As it is a direct consequence of the relative angle β between the strands, $\delta = \beta/2 = 15°$.
- The crack front angular position θ is used to define any point along the crack front. When $\theta = 0°$, the considered point is located at the crack tip, on the median plane M. On the other hand, when $\theta = -90°$ or $\theta = 90°$, the point is at the strand surface (figure 9b).

Figure 10 shows how a crack geometry is inserted into the given mesh. In this case, the crack was chosen with a "penny shape", corresponding to a disk surface. The center of this disk was placed on the hot spot location, whose coordinates were also extracted from previous simulations (figure 3). Thus, all the following section will focus on a penny shaped crack with a 400 µm radius. This geometry implies a maximum projected crack depth $b_{CA} = 200$ µm to match with the experimental crack arrest depth. It is also worth mentioning that in this configuration, $b_{CA} > l_{opt} = 130$ µm (introduced section 2.2.1.). This gives a first guarantee that gradient effects may not affect too deeply the following SIF calculations.

Finally, this model has to consider two distinct friction coefficient: the friction coefficient μ between the two aluminium strands, same as in the sane model described in the previous section, and a new friction coefficient μ_{CL} corresponding to the contact between the two crack lips. In this new configuration, both contacts were simulated using the ABAQUS Penalty algorithm. This new coefficient μ_{CL} cannot be easily

identified through experimental tests, so the first following simulations using Z-cracks will focus on the μ_{CL} influence.

For most of the next simulations, a complete fretting fatigue cycle was considered. Then, all SIF amplitudes were directly defined using the following expression:

$$\Delta K_i = K_{i,max} - K_{i,min} = K_i(Q = +Q^*) - K_i(Q = -Q^*) \quad (7)$$

When these values are mentioned to be located at the crack tip, it means that it corresponds to a crack front angular position $\theta = 0°$.

4.2. Influence of friction coefficient between the crack lips μ_{CL}

As it was earlier intuited, the crack arrest phenomena observed with fretting fatigue tests may be related to crack closure effects due to compressive hydrostatic pressure. In that context, it appears crucial to properly address the friction behavior of the crack lips themselves, as they might be in contact during a cycle and try to slide onto each other. Thus, the first SIF results presented will focus on this topic. Furthermore, shear contributions are likely to have a key role in the driving mechanisms of such cracks, which is why ΔK_{II} were specifically investigated. This will be also confirmed in the next sections.

Figure 14 shows the ΔK_{II} evolutions at the crap tip for various friction coefficients between the crack lips from $\mu_{CL} = 0$ (no friction at all) to $\mu_{CL} = 2$. For both tangential force amplitudes Q*, ΔK_{II} describes similar evolutions for a given friction coefficient μ_{CL}. In the case of no friction ($\mu_{CL} = 0$), ΔK_{II} is much higher than for any other μ_{CL}. This result can be expected as in this configuration, both lips are sliding onto each other and all the shear energy is accumulated at the front of the crack. This induces such high values for ΔK_{II}. However, this cannot be considered as a realistic hypothesis. For such a ductile and adhesive material as the studied aluminium, the crack lips cannot be assimilated as purely smooth surfaces without interaction under closure. This is why non-zero coefficients have to be considered in the modelling. On the other hand, it is interesting to note that for $\mu_{CL} \geq 0.75$, the ΔK_{II} plots describe an asymptotic decrease, and also quickly converge to the same asymptote as P increases. It means that for $P \geq P_{CA}$, ΔK_{II} is not influenced by

the friction coefficient μ_{CL}, as long as it is higher than 0.75. This last statement legitimates the arbitrary choice of μ_{CL} = 1.1 which is the same as the friction coefficient used to describe the macroscopic contact between the two strands.

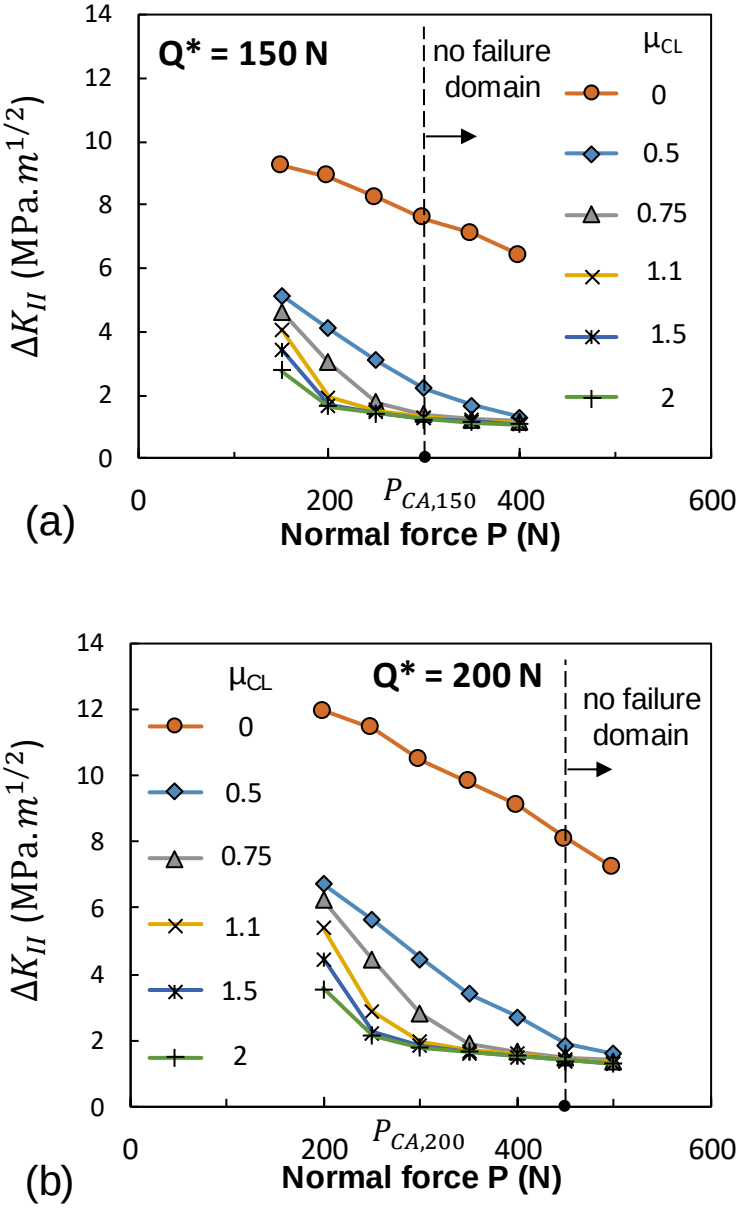

Figure 11: ΔK_{II} at the crack tip as a function of the normal force, for various friction coefficients μ_{CL} between the crack lips; (a) for Q=150 N and $\sigma_{f,max}$ = 60 MPa ; (b) for Q*=200 N and $\sigma_{f,max}$ = 60 MPa*

4.3. SIF distribution along the crack front

Figure 12 typical shows SIF distributions along the crack front with the newly defined μ_{CL} for Q = +Q* and Q = -Q*. It means that all SIF from figure 12a correspond to Ki_{max} while SIF from figure 12b are Ki_{min}. In addition to these SIF data, the normal stress σ_n was also computed by projecting the stress tensor in the vicinity of the crack tip on the normal vector of the crack surface.

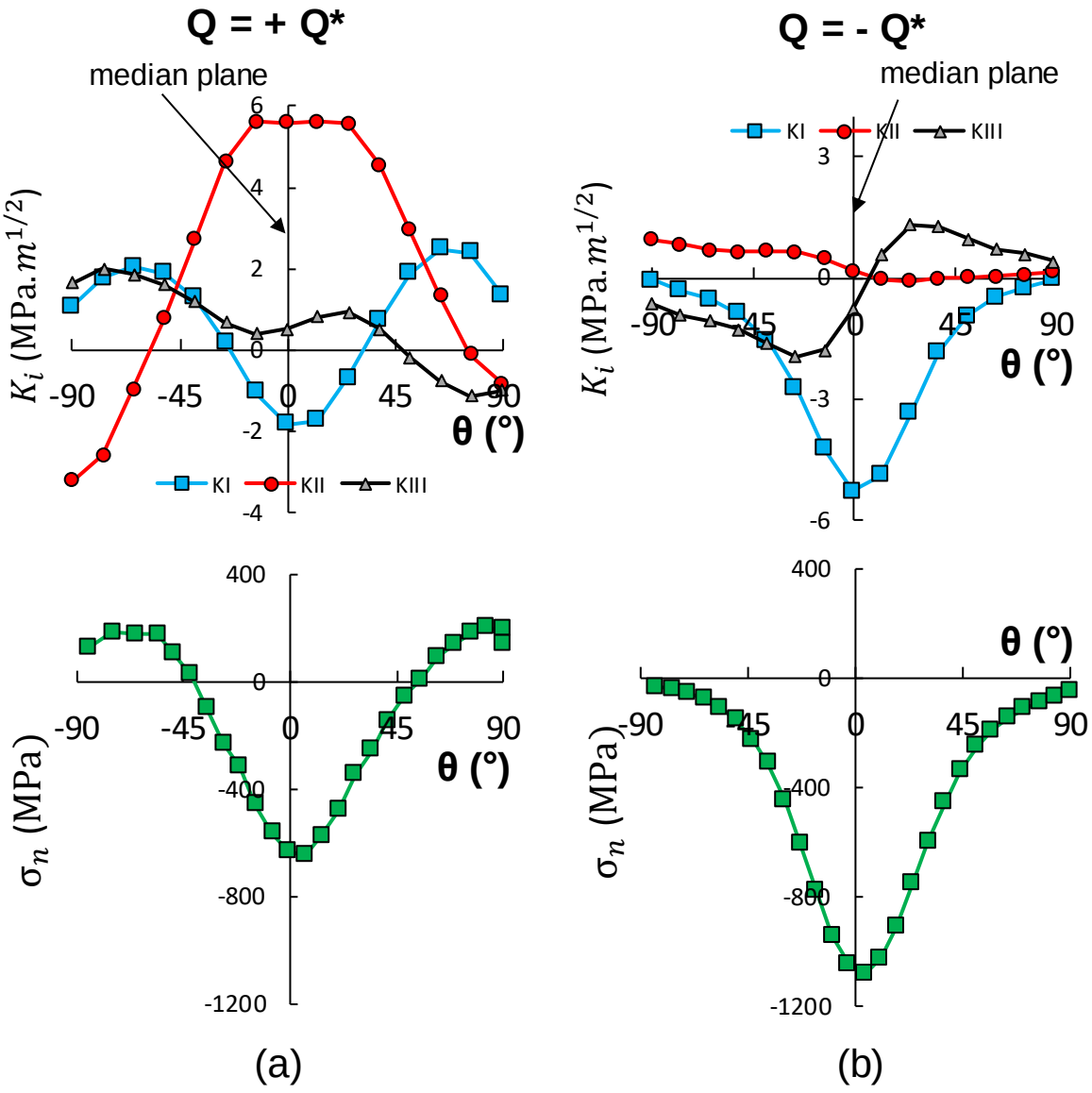

Figure 12 (a): Mode I, II and III SIF as well as normal stress σ_n distributions along the crack front at Q = +Q = 200 N and P = 300 N, $\sigma_{f,max}$ = 60 MPa; (b) distributions at Q = -Q* = -200 N and P = 300 N, $\sigma_{f,max}$ = 60 MPa*

It is interesting to note that at Q = + Q*, the K_I evolution along the crack front systematically describes a M-shaped curve, reaching its minimum in the median plane of the crack (i.e. the crack tip). This strong decrease of mode I Stress Intensity Factor is directly related to the compressive hydrostatic pressure induced by the contact. As the crack has a low diving angle $\alpha = 30°$ and its tip is right under the contact, the normal force applied by the upper counter-body directly induces high compressive stress and tends to close up the crack lips. This phenomenon is amplified at Q = - Q*, as K_I follows a sharp V-shaped evolution and the crack tip is in a fully compressive state. This first numerical results stands as a first qualitative illustration of the phenomenon observed with the fretting fatigue tests in section 3.2. It was proposed that the normal force may stop the crack propagation, and these K_I evolutions illustrates that this normal force promotes crack closure at the crack tip due to high compressive stresses. The difference of behaviors between mode I and II also illustrates the multiaxial aspect of the stress state around the crack tip, confirming the observation made in section 2.2.1.

In addition to this first statement, both plots show that $K_{I,max} < 0$ at the crack tip. It must be noted that such values do not have a physical sense and must be considered as theoretical figures based on the calculation method used. However, the choice was made to show the associated results as it gives a first estimation of the compressive state around the crack tip. Indeed, it implies that during the entire fretting cycle, the crack tip is in a compressive state. This compressive state is also confirmed by the plots of the normal stress σ_n along the crack tip. It highlights that even in such a state, K_I seems to follow similar tendencies as σ_n, with both behaviors being consistent.

Still, these observations do not mean that the crack has reached its crack arrest state: these SIF results correspond to Q = 200 N, P = 300 N, which displayed failure in fretting fatigue according to the experimental tests presented section 2.3.2. The failure can then be explained regarding the values of K_{II}, which displays a bell-shaped curve at Q = + Q* (figure 12a), reaching its maximum in the crack tip area. This highlights one of the key points of the current study: even in a fully compressive state, a crack can

propagate only driven by shear mechanisms and mode II contribution to a certain extent. It can also be observed that the crack propagates below the contact, thus its tip is located in the volume with the stronger multiaxiality (figure 3b). This highlights the fact that with these multiaxial stress conditions, with compressive mode I and strong mode II, the crack still manage to propagate while it would be impossible in any uniaxial configuration.

The following steps of the present work will then try to propose a quantification of this statement. Before that, it can be noted that $K_{Imax} > 0$ when the position is getting closer to the surface. It may suggest that the corresponding crack may propagate in mode I in these areas, unlike the crack tip. However, this hypothesis does not correspond to experimental observations, where the highest lengths are found in the median plane. This can also be explained by the fact that when closer to the surface, numerical results are more affected by fretting induced gradient effects discussed before. This is the reason why most of the presented results focus on the crack tip. In that sense and regarding K_{III} and the mode III contribution, as it displays rather low values compared to K_{II} around the crack tip, the mode III shear will be considered negligible.

As a complement of figure 12, figure 13 emphasizes on the effect of the fatigue force on the fretting induced shear behavior, as well as the normal load. It shows the ΔK_{II} evolution along the crack front for the same Q* = 200 N and two distinct normal loads: P = 250 N and P = 500 N. Both plain fretting ($\sigma_{f,max}$ = 0 MPa) and fretting-fatigue ($\sigma_{f,max}$ = 60 MPa) are compared, where the fretting-fatigue case corresponds to $\sigma_{f,max}$ = 60 MPa and R = 0.5 to remain consistent with the previous experimental results. For the lower normal load (figure 13a), the addition of fretting slightly increases ΔK_{II} especially around the crack tip at the top of the bell-shaped curve. On the other hand, for the higher P (figure 13b), fatigue doesn't seem to affect ΔK_{II} at the crack tip anymore. It is consistent with the fact that for P = 500 N, the fretting contact is far more stressing, while the fatigue bulk stress remains constant. Thus, fatigue is hardly impacting the

stress distribution in the fretting area anymore. It also confirms the experimental observation made in section 3.2., where changing the fatigue loading didn't seem to affect the crack arrest threshold.

The other key observation arising from these plots concerns the influence of the normal load itself. It highlights how an increase of normal load flattens the ΔK_{II} distribution around the crack tip, and sharply reduces its peak value. This tendency was also visible in figure 11, with the asymptotic decrease of ΔK_{II} at the crack tip when P increases. These new plots give another insight on the pressure induced crack closure. The final step is then to try to formalize the crack arrest condition based on experimental tests associated with these FEA simulations.

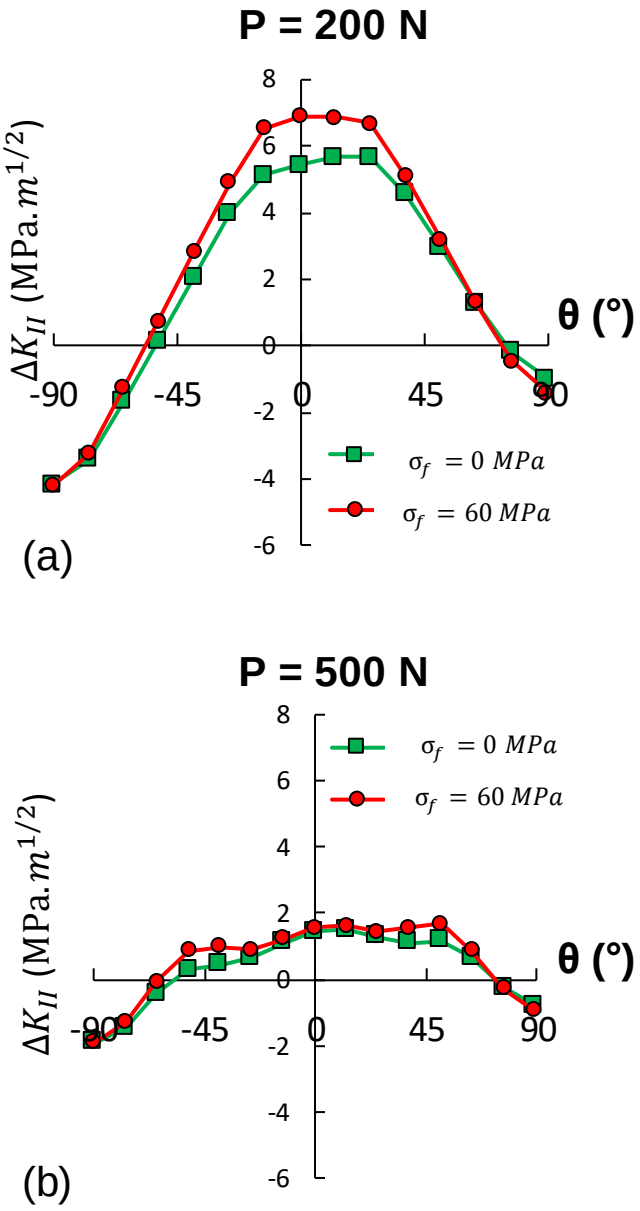

Figure 13 (a): ΔK_{II} distributions along the crack front for plain fretting (Q=200 N) and fretting fatigue (Q*=200N and $\sigma_{f,max}$ = 60 MPa) for a normal load P = 200 N; (b) same ΔK_{II} evolutions for P = 500 N*

4.4. Fretting fatigue ΔK_{II} threshold assessment

One of the most common methods to predict the crack arrest phenomenon based on SIF calculations relies on a stress intensity factor threshold noted ΔK_0. It is for instance the case when the Paris Law is applied to

model the kinetics of long cracks in a material. Whenever the equivalent ΔK_{eff} gets lower than ΔK_0, the crack is expected to stop. This methodology was also developed to account for short crack behavior, for which it was observed that even for $\Delta K_{eff} < \Delta K_0$, some propagation would still take place. A more specific SIF threshold ΔK_{th} was thus introduced. It was defined so as $\Delta K_{th} = \Delta K_0$ for long cracks and $\Delta K_{th} < \Delta K_0$ for short cracks [21]–[23]. In the latter case, ΔK_{th} would display a non-linear evolution, while it is assimilated as a material constant in the former case. However, these methods usually define their equivalent SIF ΔK_{eff} based on mode I propagation, with possible adjustments to account for shear and friction effects. In some other cases, mode II and III are further investigated, when the shear is high enough to prevent bifurcation due to the mode I contribution [24], [25]. This approach cannot be directly used in the current work: as stated in section 4.3., the studied cracks are always in compressive state. That means that the mode I equivalent SIF amplitude ΔK_{eff} would be systematically equal to zero, thus mode I cannot drive any propagation.

Before focusing specifically on the mode II mechanism when $K_{I,max} < 0$, Figure 14 illustrates how the tangential force amplitude Q* affects the conditions leading to the crack arrest. Figure 14a sums up the experimental results obtained in fretting fatigue by stressing the link between Q* and the normal force threshold P_{CA}, showing that an increase of Q* sharply raises P_{CA}. On the other hand, figure 14b puts in relevance that when $P = P_{CA}$, the ΔK_{II} value at the crack tip is not influenced by Q*. This gives a first argument to consider this specific shear SIF value $\Delta K_{II,th}$ as the threshold value to characterize the crack arrest under compressive conditions. To deepen this last statement, figure 15 insists on the ΔK_{II} behavior versus the normal force ratio P/P_{CA} for both Q*. It also introduces the normal stress $\sigma_{n,CL}$ based on the contact pressure existing between both crack lips. For every loading condition at Q = +Q*, this normal stress was averaged on the total crack lips surface, and the resulting scalar $\bar{\sigma}_{n,CL}(+Q^*)$ is plotted figure 15c. These values were obtained using a post-processing routine gathering all nodal pressures specifically between the crack lips.

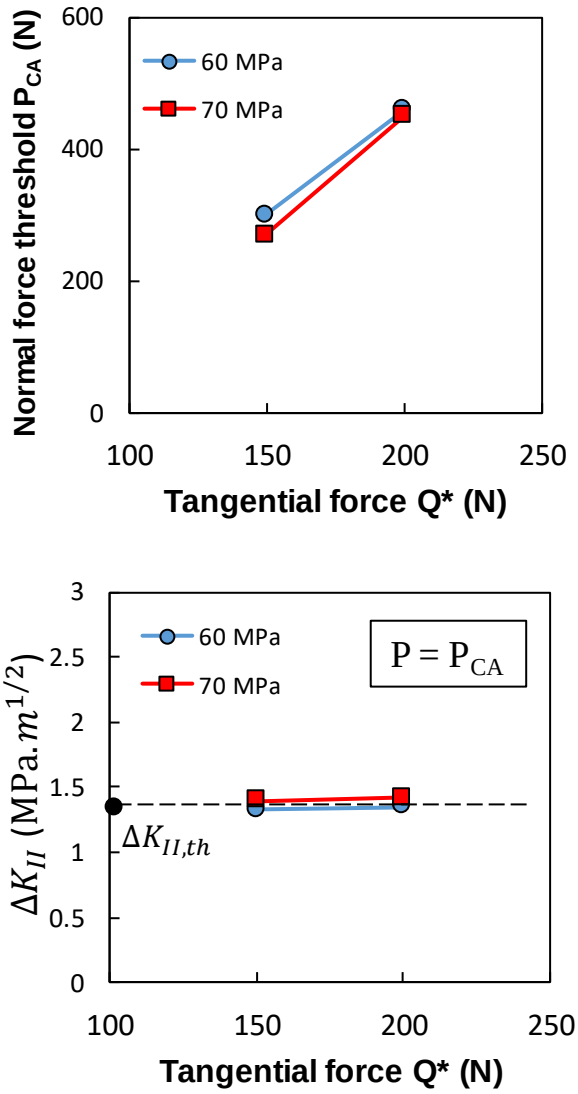

Figure 14 (a): Normal force threshold P_{CA} versus the tangential force amplitude Q; (b) ΔK_{II} evolution versus the tangential force ampliude Q* for $P = P_{CA}$*

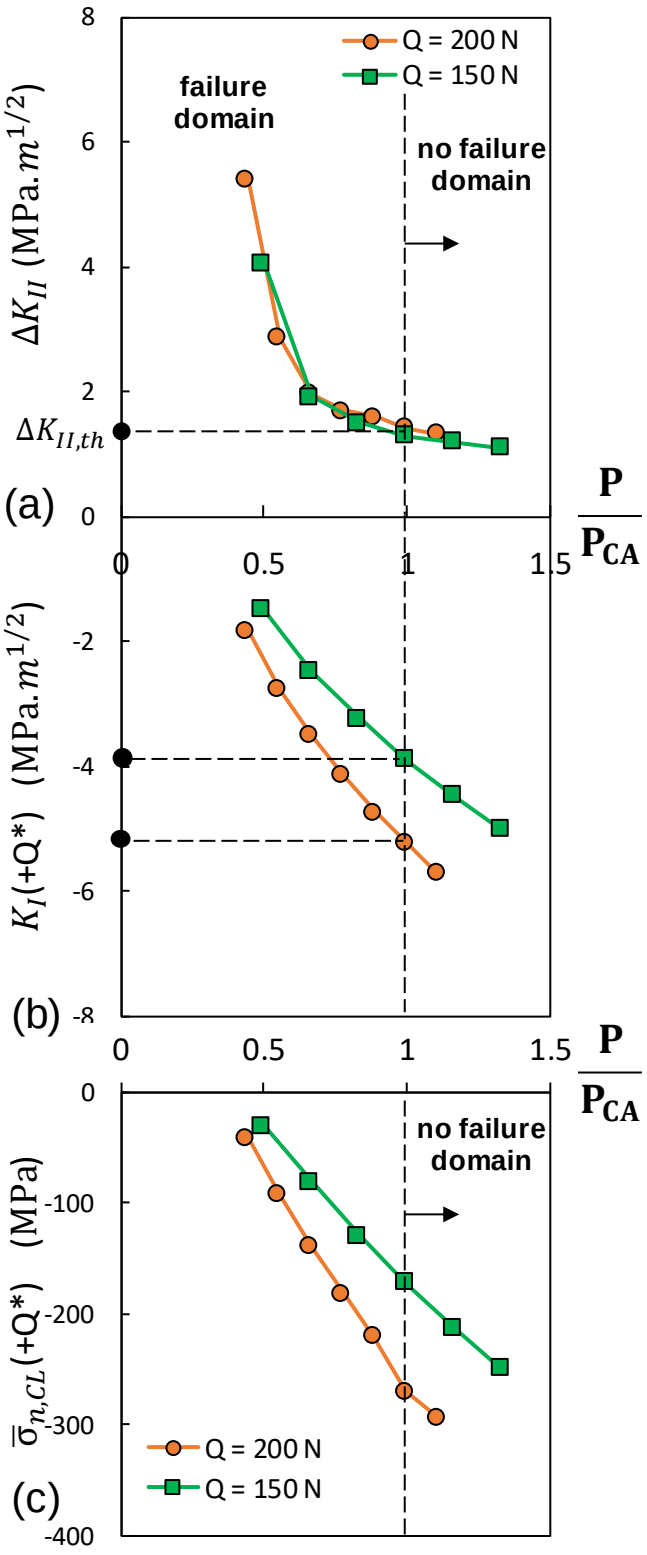

Figure 15(a): ΔK_{II} evolution versus the normal force ratio P/P_{CA} (b): $K_{I,max}$ evolutions versus the normal force ratio P/P_{CA} ; (c): averaged normal stress on the crack lips versus the normal force ratio P/P_{CA}

This way of plotting ΔK_{II} reveals that for both Q*, the shear state seen at the crack tip is very similar before and after the experimental crack arrest condition. This also gives another way of determining $\Delta K_{II,th}$, as both curves meet at ΔK_{II} = 1.35 MPa.m$^{1/2}$ approximately when P = P_{CA} (same threshold as shown in figure 14b) This can be used to propose a first empirical threshold based on this ΔK_{II} value. Furthermore, the $K_{I,max}$ evolutions in the lower part of figure 15 underline that the cracking behavior is more consistent when considering only the mode II contribution. Indeed, there is no visible condition to characterize the crack arrest by adding into consideration mode I mechanisms, and may even add more discrepancy. This may also be explained by the fact that ΔK_{II} already takes into account (indirectly) the mode I contribution through friction effects and μ_{CL}. As the crack is under closure, the contact pressure between the crack lips associated with friction affects the amount of resulting shear energy at the crack lips. Finally, the comparison between figure 15b and 15c reveals that even though K_I negative values have no physical sense, it displays very similar tendencies of evolution when compared to the evolution of the averaged pressure between the crack lips. This stands as a confirmation of the link between K_I and σ_n observed in figure 12.

The relevance of the proposed quantification can also be addressed. As seen on figure 15, the slope of the ΔK_{II} evolutions are rather low for P = P_{CA}, which can alter the accuracy of the corresponding $\Delta K_{II,th}$ value. On this regard and in order to be conservative, it appears more reliable to choose a lower value to predict the crack arrest phenomenon. These considerations help to propose a first mode II SIF threshold $\Delta K_{II,th}$ = 1.3 MPa.m$^{1/2}$ identified for this configuration. Still, the existence of the threshold itself can also give valuable hints for anyone working with materials that have been processed with coil rolling or wire drawing. It is likely that the threshold value is dependent of the aluminium strand geometry and surely the material itself, but it highlights the fact that for an equivalent sphere/plane configuration, some materials may display specific propagating mechanisms associated with the multiaxiality of loadings. These crack would only be driven by shear stresses while the sole study of the crack closure would predict no

propagation at all. Nonetheless, the previous results give an interesting insight on the propagating behavior of crack suffering lip closure, and how consistent this behavior can be.

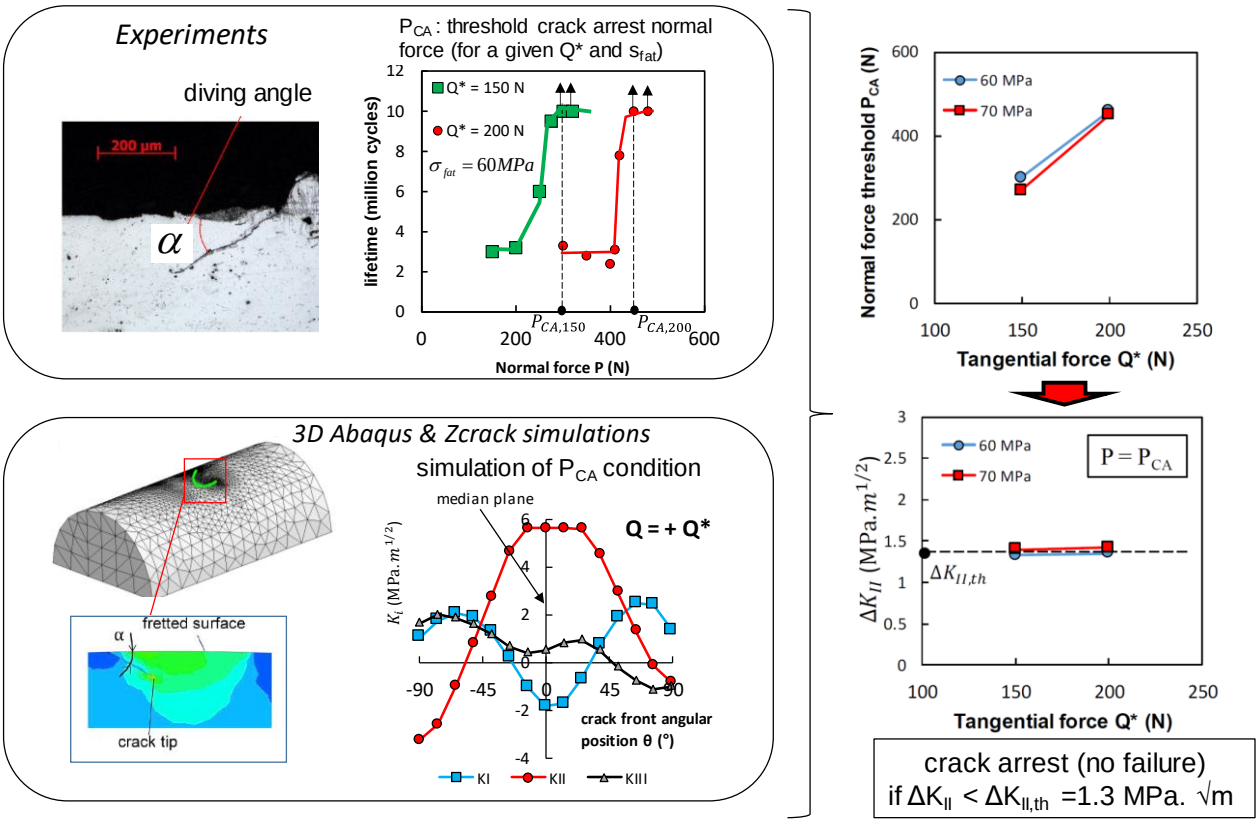

Figure 16 : recapitulative framework of the proposed approach, from experiments and simulations to the proposition of a shear SIF threshold

Conclusion

The present study proposes to extend a former methodology to account for crack propagation in addition to nucleation prediction. It was based on the initial observation that the presence of nucleated cracks in an aluminium-aluminium strand contact loaded in fretting fatigue does not guarantee the total failure in some multiaxial stress states. Thus, potential crack arrest phenomena have to be considered. Figure 16 sums up the whole methodology and emphasizes the main steps. The following aspects were exposed:

- A former multi-scale strategy to predict the fretting fatigue life of aluminium strands in an overhead conductor was described. It relies on two FEA numerical models: one to account for the global scale while the other simulate a single 3D contact. This local model was also used in the current work for Stress Intensity Factor calculations.

- Several series of experimental fretting fatigue tests were conducted to study the crack arrest occurrence only by modifying the normal force. Normal force Crack Arrest thresholds P_{CA} were deduced from these tests.

- A typical crack geometry based on optical observations on unfailed samples was defined to characterize the crack arrest state. It gave a projected crack depth b_{CA} = 200 µm and a diving angle $\alpha = 30°$.

- The Z-cracks tool was introduced to add into consideration a fully meshed crack into the numerical local model. The previously defined crack was modeled and inserted into the sane mesh, before proceeding to fretting fatigue simulations.

- The influence of the friction coefficient between the crack lips μ_{CL} has been addressed to justify the choice $\mu_{CL} = \mu = 1.1$ corresponding to an aluminium-aluminium contact previously identified.

Finally, the conclusions of the present work rely on the two following points:

- SIF distributions along the crack front reveals that this crack geometry systematically implies that the crack tip is in compressive state with $K_{I,max} < 0$. However, this does not mean that they cannot propagate further as experiments showed that for some conditions the strand total failure was still observed. This SIF analysis also highlighted the predominance of mode II shear mechanisms to explain how cracks could propagate under closure.

- Finally, a mode II SIF threshold $\Delta K_{II,th}$ = 1.3 MPa.m$^{1/2}$ was proposed to predict the crack arrest state in the given configuration.

This threshold relies on experimental results and numerical simulations and helps to understand the damage mechanisms within overhead conductors. However, the phenomenon exposed in the present study does not only apply on this specific case: such behaviors could be observed in any wire rope structure or more generally in any material having suffered coil rolling or wire drawing. Furthermore, it is also relevant for any application that involves multiaxial stress states with compression. Knowing that, it could be relevant to apply a similar strategy on any of those applications in an effort to update design decisions.

References

[1] W. G. Fricke and C. B. Rawlins, "Importance of Fretting in Vibration Failures of Stranded Conductors," *IEEE Trans. Power Appar. Syst.*, vol. 87, no. 6, pp. 1381–1384, 1968.

[2] R. B. Kalombo, J. A. Araújo, J. L. A. Ferreira, C. R. M. da Silva, R. Alencar, and A. R. Capra, "Assessment of the fatigue failure of an All Aluminium Alloy Cable (AAAC) for a 230 kV transmission line in the Center-West of Brazil," *Eng. Fail. Anal.*, vol. 61, no. August 2012, pp. 77–87, 2016.

[3] Z. R. Zhou, A. Cardou, M. Fiset, and S. Goudreau, "Fretting fatigue in electrical transmission lines," *Wear*, vol. 173, no. 1–2, pp. 179–188, 1994.

[4] S. Lalonde, R. Guilbault, and S. Langlois, "Numerical analysis of ACSR conductor-clamp systems undergoing wind-induced cyclic loads," *IEEE Trans. Power Deliv.*, vol. 33, no. 4, pp. 1518–1526, 2018.

[5] G. E. Ramey and J. S. Townsend, “Effects of clamps on fatigue of ACSR conductors,” *J. Energy Div.*, vol. 107, no. 1, pp. 103–119, 1981.

[6] A. Cardou, L. Cloutier, J. Lanteigne, and P. M’Boup, “Fatigue strength characterization of ACSR electrical conductors at suspension clamps,” *Electr. Power Syst. Res.*, vol. 19, no. 1, pp. 61–71, 1990.

[7] J. Said, S. Garcin, S. Fouvry, G. Cailletaud, C. Yang, and F. Hafid, “A multi-scale strategy to predict fretting-fatigue endurance of overhead conductors,” *Tribol. Int.*, p. 106053, 2019.

[8] S. Lalonde, R. Guilbault, and F. Légeron, “Modeling multilayered wire strands, a strategy based on 3D finite element beam-to-beam contacts - Part I: Model formulation and validation,” *Int. J. Mech. Sci.*, vol. 126, no. October, pp. 281–296, 2017.

[9] S. Lalonde, R. Guilbault, and S. Langlois, “Modeling multilayered wire strands, a strategy based on 3D finite element beam-to-beam contacts - Part II: Application to wind-induced vibration and fatigue analysis of overhead conductors,” *Int. J. Mech. Sci.*, vol. 126, no. October, pp. 297–307, 2017.

[10] A. Belkhabbaz, M. Gueguin, F. Hafid, C. Yang, J.-M. Ghidaglia, and O. Allix, “Méthodologie d’analyse fine des contacts critiques au sein d’un conducteur aérien via un modèle numérique filaire,” pp. 1–8, 2019.

[11] J. Redford, H. P. Lieurade, M. Gueguin, F. Hafid, C. Yang, and J. M. Ghidaglia, “Modélisation numérique du phénomène de fretting-fatigue intervenant dans le vieillissement des conducteurs de lignes aériennes,” *Mater. Tech.*, vol. 106, no. 3, 2018.

[12] J. A. Redford *et al.*, “Calibration of a numerical prediction methodology for fretting-fatigue crack initiation in overhead power lines,” *Int. J. Fatigue*, vol. 124, no. November 2018, pp. 400–410, 2019.

[13] S. Fouvry, P. Kapsa, F. Sidoroff, and L. Vincent, “Identification of the characteristic length scale for fatigue cracking in fretting contacts,” *J. Phys. IV JP*, vol. 8, no. 8, pp. 2–9, 1998.

[14] J. A. Araújo, L. Susmel, D. Taylor, J. C. T. Ferro, and J. L. A. Ferreira, “On the prediction of high-cycle fretting fatigue strength: Theory of critical distances vs. hot-spot approach,” *Eng. Fract. Mech.*, vol. 75, no. 7, pp. 1763–1778, 2008.

[15] C. Gandiolle and S. Fouvry, “Stability of critical distance approach to predict fretting fatigue cracking: A "ℓ opt -b opt " concept,” *Int. J. Fatigue*, vol. 82, pp. 199–210, 2016.

[16] R. Ferré, S. Fouvry, B. Berthel, and J. A. Ruiz-Sabariego, “Stress gradient effect on the crack nucleation process of a Ti-6Al-4V titanium alloy under fretting loading: Comparison between non-local fatigue approaches,” *Int. J. Fatigue*, vol. 54, pp. 56–67, 2013.

[17] I. V. Papadopoulos and V. P. Panoskaltsis, “Invariant formulation of a gradient dependent multiaxial high-cycle fatigue criterion,” *Eng. Fract. Mech.*, vol. 55, no. 4, pp. 513–528, 1996.

[18] R. Amargier, S. Fouvry, L. Chambon, C. Schwob, and C. Poupon, “Stress gradient effect on crack initiation in fretting using a multiaxial fatigue framework,” *Int. J. Fatigue*, vol. 32, no. 12, pp. 1904–1912, 2010.

[19] S. Geniaut, P. Massin, and N. Moes, “Evaluation of stress intensity factors with G-theta method and level sets in Code-Aster,” *11th Int. Conf. Fract. 2005, ICF11*, vol. 2, pp. 1043–1048, 2005.

[20] P. Destuynder and M. Djaoua, “Sur une interpretation mathematique de l’integrale de Rice en theorie de la rupture fragile,” *Math. Meth. Appl. Sci.*, vol. 3, pp. 70–87, 1981.

[21] K. J. MILLER, “the Short Crack Problem,” *Fatigue Fract. Eng. Mater. Struct.*, vol. 5, no. 3, pp. 223–232, 1982.

[22] A. de Pannemaecker, S. Fouvry, and J. Y. Buffiere, “Reverse identification of short-long crack threshold fatigue stress intensity factors from plain fretting crack arrest analysis,” *Eng. Fract.*

Mech., vol. 134, pp. 267–285, 2015.

[23] A. De Pannemaecker, S. Fouvry, and J. Y. Buffiere, “Introduction of a reverse simulation approach to identify the fatigue stress intensity factor crack arrest threshold from fretting cracking experiments,” *Tribol. Int.*, vol. 76, pp. 122–132, 2014.

[24] V. Doquet, Q. H. Bui, G. Bertolino, E. Merhy, and L. Alves, “3D shear-mode fatigue crack growth in maraging steel and Ti-6Al-4V,” *Int. J. Fract.*, vol. 165, no. 1, pp. 61–76, 2010.

[25] A. Otsuka and K. Mori, “Mode II fatigue crack growth in aluminium alloys and mild steel,” *Curr Jpn Mat Res 1*. pp. 149–180, 1987.